ACS APPLIED BIO MATERIALS

www.acsabm.org Article

Lysosome Targeting Bis-terpyridine Ruthenium(II) Complexes: Photophysical Properties and *In Vitro* Photodynamic Therapy

Bingqing Liu,[§] Yibo Gao,[§] Mohammed A. Jabed, Svetlana Kilina, Guoquan Liu,* and Wenfang Sun*

Cite This: *ACS Appl. Bio Mater.* 2020, 3, 6025−6038 Read Online

ACCESS | Metrics & More | Article Recommendations | Supporting Information

ABSTRACT: Three heteroleptic bis-terpyridine ruthenium(II) complexes (**Ru1**−**Ru3**) $[Ru(tpy\text{-}R_1)(tpy\text{-}R_2)]^{2+}$ (tpy = 2,2′:6′,2″-terpyridine, R_1/R_2 = phenyl, 4-{2-[2-(2-methoxyethoxy)ethoxy]ethoxy}phenyl, pyren-1-yl, or 4-phenyl-BODIPY (boron dipyrromethene)) were synthesized and investigated for their potential applications as photosensitizers (PSs) for photodynamic therapy. All complexes displayed broad and intense absorption band in the green spectral regions (450−600 nm), which arose from the spin-allowed charge-transfer transitions mixed with ligand-localized $^1\pi,\pi^*$ transitions. All complexes show weak green emission at 513−549 nm and/or even weaker red emission at 646−674 nm at room temperature depending on the excitation wavelength and the solvent used. Incorporating the BODIPY motif to the 4′-position of one of the tpy ligands in **Ru2** and **Ru3** drastically prolonged the lifetimes of the lowest triplet excited states (T_1) of **Ru2** and **Ru3** to tens of microseconds. This promoted the singlet oxygen formation sensitized by **Ru2** and **Ru3** upon green light activation, which in turn induced significant photocytotoxicity toward the A549 human lung cancer cell line with an EC_{50} value of 1.50 μM for **Ru2** and 7.41 μM for **Ru3** under 0.48 J·cm^{-2} 500 nm light irradiation. Laser confocal scanning microscopy imaging revealed that **Ru2** mainly distributed to lysosomes upon cell uptake. Upon 500 nm light activation, **Ru2** induced lysosomal damage and subsequent mitochondrial membrane potential decrease. The dominant cell death pathway was apoptosis. These results demonstrated the potential utilization of $[Ru(tpy\text{-}R_1)(tpy\text{-}R_2)]^{2+}$ complexes as PSs for PDT.

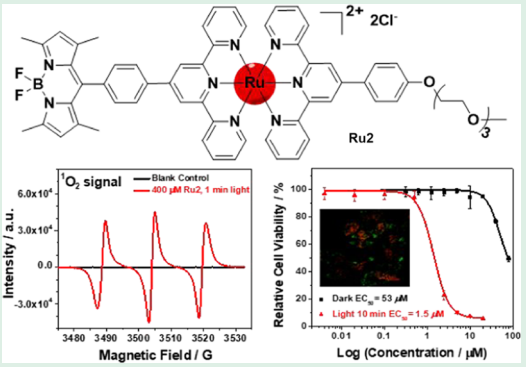

KEYWORDS: *bis-terpyridine ruthenium(II) complex, photophysics, photodynamic therapy, reactive oxygen species, singlet oxygen, absorption, emission, transient absorption*

INTRODUCTION

Photodynamic therapy (PDT) is a noninvasive cancer treatment modality, which induced cell death upon light activation of an otherwise nontoxic drug (i.e., photosensitizer (PS)) in the presence of adequate oxygen.[1−3] The effectiveness of PDT is directly related to the yield of toxic reactive oxygen species (ROS) generated by either electron (type I) or energy transfer (type II) from the triplet excited state of a PS to the surrounding ground-state oxygen ($^3O_2$). Thus, PSs holding long-lived triplet excited states and high quantum yields of triplet excited state formation to facilitate ROS production in high yields are highly desirable. To date, PDT is mainly utilized to treat superficial tumors because the PSs in clinical use are unable to efficiently absorb the low-energy, tissue-penetrating red to near-infrared (NIR) light.[1,4] Considering the potential clinical applications of PDT for treating deeply seated tumors in the future, PSs with strong absorption in the red to NIR spectral regions and long-lived triplet excited states are highly needed.

Compared to the organic PSs currently in clinical use or in clinical trials, d-block heavy transition-metal complexes, such as Ru(II), Os(II), Pt(II), and Ir(III) complexes, hold great potential as PSs for PDT due to their high quantum efficiency for triplet excited state formation.[1,3,5−10] Among them, pseudo-octahedral Ru(II) complexes have been receiving longstanding attention as anticancer drugs including as PSs for PDT[1,5−9,11−13] owing to their chemical and photochemical stability, interesting photophysical properties, and structural diversity.[14−18] Ru(II) complex TLD1433,[1,9] a $[Ru(N^\wedge N)_2(N^\wedge N)']^{2+}$-type complex (N^N refers to the diimine ligands) incorporating an α-terthienyl-substituted imidazo[4,5-*f*][1,10]phenanthroline ligand has successfully completed the phase 1 human clinical trials for treating bladder cancer with PDT and is currently in phase 2 trials (ClinicalTrials.gov Identifier NCT03945162). This demonstrates the great potential of utilizing Ru(II) complexes for PDT. However, most of the reported Ru(II) complex-based PSs for PDT bear

Received: May 29, 2020
Accepted: August 7, 2020
Published: August 7, 2020

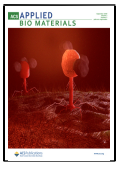

https://dx.doi.org/10.1021/acsabm.0c00647
ACS Appl. Bio Mater. 2020, 3, 6025−6038

tris-diimine ligands.[1,5−9,19] Exploration of Ru(II) bis-terdentate complexes such as Ru(R-tpy)$_2^{2+}$ (tpy refers to 2,2′:6′,2″-terpyridine) for PDT has been very rare.[5,9,11,20−22]

Differing from the Ru(II) complexes containing tris-diimine ligands, Ru(R-tpy)$_2^{2+}$ complexes have the advantages of avoiding formation of geometric isomers when the modification is done at the 4′-position of tpy, which may reduce the synthetic challenges for developing new Ru(II) complexes to tailor a specific application.[23] This type of Ru(II) complexes also exhibited relatively strong metal-to-ligand charge transfer (^{1}MLCT) absorption in the visible spectral regions (450−600 nm). However, the distorted coordination angles of tpy to the Ru(II) ion led to a weaker ligand field strength, facilitating the thermally activated decay pathway associated with the low-lying metal-centered (^{3}MC) excited state.[18] Consequently, the Ru(R-tpy)$_2^{2+}$ complexes typically possess extremely short-lived triplet excited states, which hamper the utilization of this type of Ru(II) complexes as PSs for PDT.

It has been reported that bichromophoric Ru(II) complexes tethered with π-conjugated organic chromophores exhibited long-lived $^3\pi,\pi^*$ states localized on the organic chromophore as the lowest triplet excited states (T_1), while the ground-state absorption was bathochromically shifted to longer wavelengths.[8,19,24−29] This strategy has been applied and well studied in Ru(II) tris-diimine complexes[8,19,24−26] but relatively rare for Ru(R-tpy)$_2^{2+}$-type complexes.[27−29] To the best of our knowledge, the only reported work on applying this strategy to Ru(R-tpy)$_2^{2+}$-type complexes were by Ziessel's[27,28] and Hanan's[29] groups. In Ziessel's work, they attached 4,4-difluoro-4-bora-3a,4a-diaza-s-indacene (or boron dipyrromethene (BODIPY)) to one of the tpy ligands to switch the T_1 state of the resultant Ru(II) complexes to the long-lived (8−30 μs) BODIPY-localized $^3\pi,\pi^*$ states. In addition, the intense absorption of BODIPY in the visible spectral regions (≥480 nm) drastically increased the absorption of the Ru(II) complexes at 400−600 nm.[27,28] In Hanan's work, 4-(anthracen-9-yl)pyrimidine motif was introduced to one or two tpy ligand(s) to extend the emission lifetime of [(an-pym-tpy)Ru(tpy-pym-an)](PF$_6$)$_2$ to ∼1.8 μs, with the lowest triplet excited state being the $^3\pi,\pi^*$ state of anthracene.[29] However, no applications of these complexes have ever been explored.

As demonstrated by Ziessel's and others' work, BODIPY and its derivatives, the visible-light-harvesting chromophores, can be attached to the scaffold of PSs to access the strong absorption in the visible spectral regions.[27,28,30−33] Meanwhile, attaching BODIPY on the ligand could extend the π-conjugation of the ligand and induce a low-lying $^3\pi,\pi^*$ state in the complex to increase the lifetime of its T_1 state.[30−33] Except for BODIPY, pyrene is another type of organic chromophore that has been frequently attached to transition-metal complexes to extend the triplet excited state lifetime because of the extremely long-lived and low-lying pyrene-based $^3\pi,\pi^*$ state. This strategy has been manifested in tris-diimine Ru(II) complexes,[25] tris-cyclometalating Ir(III) complexes,[34] and bis-tpy Ir(III) complexes.[35] However, attaching pyrene, especially both the pyrene and BODIPY motifs to the tpy ligands for preparation of Ru(R-tpy)$_2^{2+}$-type complexes for PDT applications has never been explored.

With the aforementioned background in mind, we developed three mononuclear [Ru(tpy-R$_1$)(tpy-R$_2$)]$^{2+}$ complexes (**Ru1**−**Ru3**, Chart 1), where R$_1$ = 4-{2-[2-(2-methoxyethoxy)ethoxy]ethoxy}phenyl and R$_2$ = phenyl (**Ru1**), R$_1$ = 4-{2-[2-(2-methoxyethoxy)ethoxy]ethoxy}phenyl and R$_2$ = 4-BODIPY-phenyl- (**Ru2**), and R$_1$ = pyren-1-yl and R$_2$ = 4-BODIPY-phenyl (**Ru3**), as photosensitizers for *in vitro* PDT. Different substituents on the tpy ligand were employed to tune the photophysical characteristics and photosensitizing capacities. Besides, the oligoether chain was utilized in complexes **Ru1** and **Ru2** to improve the solubility of these complexes in aqueous solutions. The tethered BODIPY and pyrene moieties in **Ru2** and **Ru3** were used to switch the T_1 states in these complexes to the BODIPY or pyrene-localized $^3\pi,\pi^*$ state and thus prolong the T_1 lifetimes of these complexes.

Chart 1. Molecular Structures of Ru(II) Complexes Ru1−Ru3

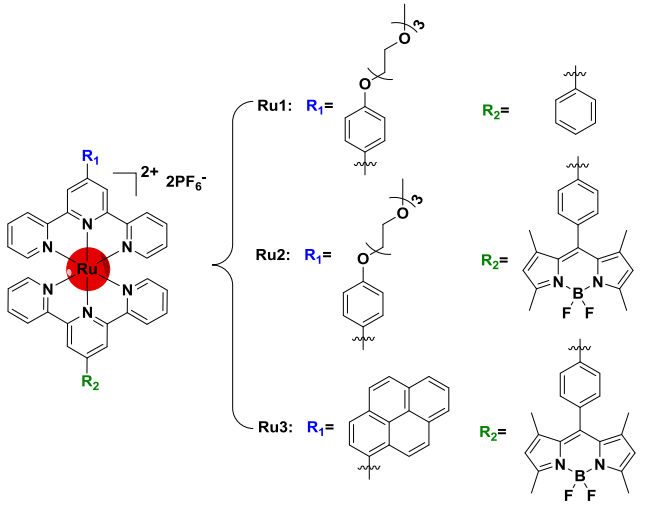

EXPERIMENTAL SECTION

Materials and Synthesis. All reagents and solvents were purchased from commercial sources and used as received. 4-{4′-{2-[2-(2-Methoxyethoxy)ethoxy]ethoxy}phenyl}tpy and 4-(pyren-1-yl)tpy were synthesized according to the literature procedures.[35−37] The synthetic routes for precursor compounds **1**−**4** and complexes **Ru1**−**Ru3** are shown in Scheme 1. These complexes were characterized by ^{1}H NMR spectroscopy, high-resolution mass spectrometry (HRMS), and elemental analyses. The ^{1}H NMR spectra were recorded on a Bruker-400 spectrometer using tetramethylsilane (TMS) as the internal standard. Electrospray ionization (ESI)-HRMS analysis was conducted on a Waters Synapt G2-Si mass spectrometer. The elemental analyses were performed at NuMega Resonance Laboratories, Inc. in San Diego, California. The ^{1}H NMR and ESI−HRMS spectra for **Ru1**−**Ru3** are provided in the Supporting Information Figures S1 and S2.

Synthesis of Precursor Compounds 1−4. *Compound 1.* At 0 °C, NaBH$_4$ (175 mg, 4.6 mmol) was added to a solution of terephthalaldehyde (2.5 g, 18.5 mmol) in EtOH (30 mL) and THF (30 mL) under vigorous stirring for 6 h. Then, the mixture was neutralized to pH 5 by diluted hydrochloric acid, and the organic solvents were evaporated. Ethyl acetate was added to extract the organic materials. The obtained crude product was purified by column chromatography eluted with ethyl acetate and hexane (2:1, v/v) to afford a white solid as the target compound (1.82 g, 89%). ^{1}H NMR (500 MHz, CDCl$_3$): δ 9.99 (s, 1H), 7.87 (d, J = 8.1 Hz, 2H), 7.53 (d, J = 8.0 Hz, 2H), 4.80 (s, 2H).

Compound 2. Compound **1** (2.72 g, 40 mmol), 2-acetylpyridine (4.84 g, 20 mmol), and KOH (2.24 g, 40 mmol) were mixed in EtOH (100 mL), and the mixture was stirred at r.t. for 2 h. After that, ammonium hydroxide (28%, 30 mL) was added into the mixture, and the mixture was heated to reflux for 24 h. After cooling to r.t., the white precipitate was collected via filtration and washed with 95%

https://dx.doi.org/10.1021/acsabm.0c00647
ACS Appl. Bio Mater. 2020, 3, 6025−6038

Scheme 1. Synthetic Routes for Compounds 1−4 and Complexes Ru1−Ru3[a]

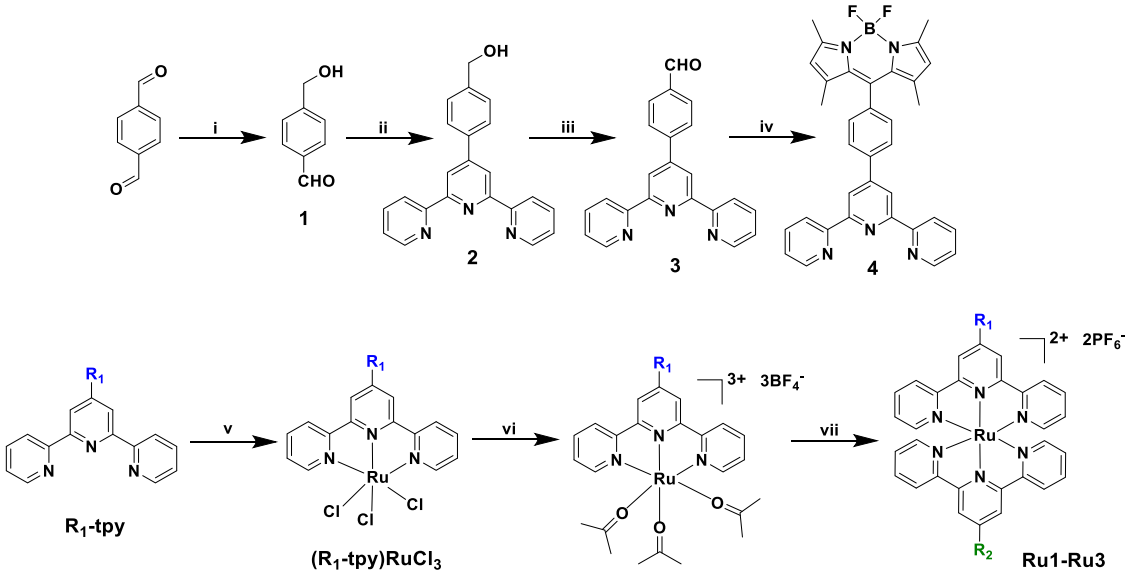

[a]Reagents and conditions: (i) $NaBH_4$, ethanol, tetrahydrofuran (THF), 0 °C, 6 h; (ii) 2-acetylpyridine, KOH, $NH_3·H_2O$, ethanol, reflux, 24 h; (iii) MnO_2, chloroform, r.t., 3 days; (iv) 2,4-dimethylpyrrole, TFA (cat.), dichloromethane, r.t., 12 h; 2,3-dichloro-5,6-dicyanobenzoquinone (DDQ), r.t., 15 min; then $BF_3·OEt_2$, Et_3N, r.t., 3 h; (v) $RuCl_3·3H_2O$, EtOH, reflux, overnight; (vi) $AgBF_4$, acetone, reflux, 3 h; (vii) corresponding R_2-tpy ligand, NH_4PF_6, ethanol, reflux, 24 h.

ethanol. The crude product was recrystallized in 95% ethanol to give compound **2** as a white solid (2.78 g, 41%). ^{1}H NMR (400 MHz, $CDCl_3$): δ 8.81−8.74 (m, 4H), 8.70 (dt, J = 8.0, 1.1 Hz, 2H), 7.97−7.88 (m, 4H), 7.54 (dd, J = 8.0, 0.5 Hz, 2H), 7.38 (ddd, J = 7.5, 4.8, 1.2 Hz, 2H), 4.82 (d, J = 5.8 Hz, 2H).

Compound ***3***. Compound **2** (1.00 g, 2.95 mmol) was dissolved in 300 mL of chloroform. Then, 20 equiv of MnO_2 (4.85 g, 60 mmol) was added. Following the thin-layer chromatography (TLC) monitoring, the oxidation reaction was essentially completed after 3 days. The black suspension was filtered, and the solvent in the filtrate was evaporated. The obtained white solid was pure enough without further purification (870 mg, 87%). ^{1}H NMR (400 MHz, $CDCl_3$): δ 10.12 (s, 1H), 8.78 (s, 2H), 8.74 (ddd, J = 4.8, 1.8, 0.9 Hz, 2H), 8.69 (dt, J = 8.0, 1.0 Hz, 2H), 8.14−7.98 (m, 4H), 7.95−7.84 (m, 2H), 7.38 (ddd, J = 7.5, 4.8, 1.2 Hz, 2H).

Compound ***4***. 2,4-Dimethylpyrrole (190 mg, 2 mmol) and compound **3** (337 mg, 1 mmol) were dissolved in CH_2Cl_2 with a catalytic amount of TFA (2−3 drops). The mixture was stirred for 12 h at room temperature. Then, a solution of 2,3-dichloro-5,6-dicyanobenzoquinone (227 mg, 1 mmol) in CH_2Cl_2 was added dropwise, and the mixture was stirred at r.t. for 15 min. Finally, $BF_3·OEt_2$ (2 mL) and triethylamine (20 mL) were added, and the obtained mixture was stirred for another 3 h at room temperature. The crude mixture was diluted with CH_2Cl_2 and washed with H_2O. The organic extracts were dried over $MgSO_4$, filtered, and evaporated under reduced pressure. The crude product was purified via flash chromatography on silica gel eluted with hexane and dichloromethane (1:1, v/v) to afford compound **4** as a red solid (280 mg, 51%). ^{1}H NMR (400 MHz, $CDCl_3$): δ 8.79 (s, 2H), 8.75 (ddd, J = 4.8, 1.8, 0.9 Hz, 2H), 8.71 (dt, J = 8.0, 1.1 Hz, 2H), 8.06−8.02 (m, 2H), 7.94−7.89 (m, 2H), 7.48−7.43 (m, 2H), 7.39 (ddd, J = 7.5, 4.8, 1.2 Hz, 2H), 6.01 (s, 2H), 2.58 (s, 6H), 1.46 (s, 6H).

General Synthetic Procedure for Precursors and Complexes Ru1−Ru3. $RuCl_3·3H_2O$ (261 mg, 1 mmol) and R_1-tpy (1 mmol) in EtOH (10 mL) were heated to reflux under a nitrogen atmosphere overnight. After the mixture was cooled to room temperature, the precipitate was collected by centrifugation and washed with EtOH, H_2O, and ether (20 mL × 2 each). The dark red solid was dried under vacuum to get a pure product without further purification.

A suspension of the corresponding (R_1-tpy)$RuCl_3$ (0.05 mmol), $AgBF_4$ (39 mg, 0.2 mmol), and acetone (10 mL) was heated to reflux for 3 h in the dark under a nitrogen atmosphere. The obtained dark green suspension was filtered by Celite to remove AgCl and dried under vacuum to remove acetone. Then, ethanol (20 mL) and R_2-tpy (0.05 mmol) were added to the solution and the mixture was heated to reflux for 24 h in the dark under nitrogen. After removal of the solvent, the residue was redissolved in acetonitrile, and the solution was added dropwise to the saturated aqueous solution of NH_4PF_6. The resulting PF_6^- salt precipitate was washed with water and purified by chromatography on an Al_2O_3 column; gradient elution from CH_2Cl_2 to acetone/H_2O (95:5, v/v) yielded the target complex. The reported yield for each Ru(II) complex is for the two-step reactions based on the R_1-tpy ligand. To obtain the Cl^- salts of **Ru1−Ru3** for the electron paramagnetic resonance (EPR) measurements and (photo)biological studies, anion exchange was conducted using Amberlite IRA-410 ion exchange resin, with methanol being used as the eluent.

Ru1. Red solid (yield: 51%). ^{1}H NMR (400 MHz, acetone-d_6): δ 9.43 (d, J = 9.8 Hz, 4H), 9.07 (dd, J = 8.0, 4.1 Hz, 4H), 8.33 (d, J = 8.8 Hz, 4H), 8.15−8.06 (m, 4H), 7.83 (dd, J = 12.2, 5.1 Hz, 4H), 7.77 (t, J = 7.4 Hz, 2H), 7.70 (d, J = 7.4 Hz, 1H), 7.41−7.30 (m, 6H), 4.37−4.31 (m, 2H), 3.95−3.91 (m, 2H), 3.75−3.70 (m, 2H), 3.69−3.65 (m, 2H), 3.63 (dd, J = 5.7, 3.9 Hz, 2H), 3.52 (dd, J = 5.7, 3.9 Hz, 2H), 3.32 (s, 3H). ESI−HRMS (m/z): calcd. for $[C_{49}H_{44}N_6O_4Ru]^{2+}$, 441.1241; found, 441.1241. Anal. Calcd (%) for $C_{49}H_{44}F_{12}N_6O_4P_2Ru$: C, 50.22; H, 3.78; N, 7.17. Found: C, 50.10; H, 4.14; N, 7.28.

Ru2. Red solid (yield: 20%). ^{1}H NMR (400 MHz, acetone-d_6): δ 9.62 (s, 2H), 9.42 (s, 2H), 9.12 (d, J = 7.9 Hz, 2H), 9.07 (d, J = 7.7 Hz, 2H), 8.64 (d, J = 8.3 Hz, 2H), 8.34 (d, J = 8.7 Hz, 2H), 8.11 (dd, J = 6.5, 4.5 Hz, 4H), 7.86 (dd, J = 15.3, 8.3 Hz, 6H), 7.44−7.22 (m, 6H), 6.21 (s, 2H), 4.39−4.28 (m, 2H), 3.98−3.88 (m, 2H), 3.78−3.70 (m, 2H), 3.69−3.57 (m, 4H), 3.55−3.43 (m, 2H), 3.32 (s, 3H), 2.56 (s, 6H), 1.60 (s, 6H). ESI−HRMS (m/z): calcd. for $[C_{62}H_{57}BF_2N_8O_4Ru]^{2+}$, 564.1816; found, 564.1805. Anal. Calcd (%) for $C_{62}H_{57}BF_{14}N_8O_4P_2Ru·3.5H_2O$: C, 50.28; H, 4.36; N, 7.57. Found: C, 50.22; H, 4.11; N, 7.85.

Ru3. Red solid (yield: 33%). ^{1}H NMR (400 MHz, acetone-d_6): δ 9.61 (s, 2H), 9.44 (s, 2H), 9.11 (d, J = 8.2 Hz, 2H), 9.04 (d, J = 8.1 Hz, 2H), 8.72−8.61 (m, 4H), 8.53−8.43 (m, 3H), 8.41−8.34 (m, 3H), 8.25−8.21 (m, 1H), 8.18−8.08 (m, 4H), 8.01 (d, J = 5.7 Hz, 2H), 7.96 (d, J = 7.9 Hz, 2H), 7.90 (d, J = 5.4 Hz, 2H), 7.45 (dd, J = 6.8, 6.0 Hz, 2H), 7.38 (dd, J = 7.3, 5.8 Hz, 2H), 6.66 (s, 2H), 2.59 (s,

https://dx.doi.org/10.1021/acsabm.0c00647
ACS Appl. Bio Mater. 2020, 3, 6025−6038

6H), 1.70 (s, 6H). ESI−HRMS (m/z): calcd. for $[C_{65}H_{47}BF_2N_8Ru]^{2+}$, 545.1526; found, 545.1513. Anal. Calcd (%) for $C_{65}H_{47}BF_{14}N_8P_2Ru\cdot 3.3CH_2Cl_2$: C, 49.41; H, 3.25; N, 6.75. Found: C, 49.32; H, 3.05; N, 6.98.

Photophysical Studies. The PF_6^- salts of **Ru1**−**Ru3** were used for the photophysical studies because of their better solubility in organic solvents. The electronic absorption spectra were recorded on a Varian Cary 50 spectrophotometer. Emission spectra were measured on a HORIBA FluoroMax 4 fluorometer/phosphorometer. Using the relative actinometry method,[38] emission quantum yields of **Ru1**−**Ru3** were deduced using $[Ru(bpy)_3]Cl_2$ in degassed acetonitrile (λ_{max} = 436 nm, Φ_{em} = 0.097)[39] as the reference. The nanosecond transient absorption (TA) data, including the TA spectra and triplet lifetimes, were measured in nitrogen-purged (~40 min) acetonitrile solutions on a laser flash photolysis spectrometer (Edinburgh LP920). A 355 nm third-harmonic output of a Quantel Brilliant Nd:YAG laser with 4.1 ns pulsewidth and 1 Hz repetition rate was used as the excitation source.

For evaluation of the singlet oxygen generation quantum yields of **Ru1**−**Ru3** in air-saturated CH_3CN, the comparative method was employed with $[Ru(bpy)_3]Cl_2$ in aerated CH_3CN (Φ_Δ = 0.57)[40] being used as the reference complex. The instrument used was an Edinburgh TL900 transient luminescence spectrometer that was equipped with an EI-P Germanium detector to monitor the emission of the singlet oxygen at 1270 nm. To eliminate the scattered light from the laser, a silicon cutoff filter (>1100 nm) was used. The excitation source was the third-harmonic output (355 nm) of a Quantel Nd:YAG laser. The singlet oxygen emission intensity at zero time delay was measured and compared to that of the optically matched (A_{355nm} = 0.5 in a 1 cm cuvette) reference complex under the identical excitation condition. The following equation was applied to calculate the Φ_Δ[40]

$$\Phi_\Delta^s = \Phi_\Delta^{ref} \times \frac{I_0^s}{I_0^{ref}} \times \frac{A_{ref}}{A_s} \times \left(\frac{n_s}{n_{ref}}\right)^2$$

where I_0 is the singlet oxygen emission intensity at t = 0, A is the absorbance at 355 nm in a 1 cm cuvette, n is the refractive index of the solvent, and the suffixes "s" and "ref" stand for the sample and the reference, respectively.

Computational Methodologies and Details. Density functional theory (DFT)[41] was utilized to optimize the ground-state singlet geometry of the complexes using the PBE0 functional.[42] The LANL2DZ basis set[43] with incorporated core pseudopotentials was used for Ru(II), and the 6-31G* basis set[44] was used for remaining atoms. The effects of the solvent (acetonitrile) were considered via the conductor-like polarizable continuum model (CPCM)[45] in both geometry optimizations and excited-state calculations. Vertical excitation energy and their oscillation strength were calculated using linear response time-dependent DFT (TDDFT)[46] with the same functional and mixed LANL2DZ/6-31G* basis set as for the ground-state calculations. The calculated absorption spectral profile was generated using the Gaussian distribution function with 0.08 eV line width to mimic the thermal broadening of the spectra.

The calculated absorption spectra of all complexes followed a qualitative trend with experimental absorption spectra, while the optical transitions were blue-shifted by about 0.4 eV. This is a well-known problem[47,48] of the hybrid-type functionals such as PBE0, where the addition of 25% of Hartree−Fock (HF) exchange to the exchange−correlation term does not completely resolve the spurious self-interaction problem,[49,50] leading to failures in energies of excitations with the long-range charge-transfer character.[51,52] To correct this behavior, we applied a scissor operator approach, which is a common practice in solid-phase calculations,[53] with all calculated spectra being red-shifted by a constant of 0.4 eV. This shift resulted in a good agreement between the calculated and experimental spectra for the studied complexes.

To calculate the phosphorescence energies, the lowest-energy excited state with the triplet spin multiplicity was optimized using an analytical gradient TDDFT method[54] by applying the same functional and basis sets as in the ground-state calculations. The nature of the electronic transitions was predicted by the natural transition orbitals (NTOs),[55] which showed the spatial charge density distribution of the electron−hole pair contributing to the optical transition. All calculations were done in Gaussian16 software packages,[56] and all NTO images were plotted in VMD visualization software.[57]

Electron Paramagnetic Resonance (EPR) Measurements. EPR spectroscopy was used to investigate the generation of free radicals upon light activation. **Ru2** or **Ru3** was dissolved in a mixture of water and acetonitrile (1:4, v/v) with 100 mM 4-OH-TEMP (radical scavenger) and irradiated with a 532 nm light of 200 mW·cm^{-2}. The mixture was measured on a Bruker A200 X band EPR spectrometer after light irradiation at room temperature. The standard parameters for EPR measurements were set as follows: microwave power = 1.62 mW, modulation frequency = 100.00 kHz, modulation amplitude = 1.00 G, sweep field width = 60 G, and sweep time = 60 s.

Cell Culture. A549 cells were obtained from Siwang Yu (Peking University, School of Pharmaceutical Sciences, Beijing, People's Republic of China) and have been proven to be negative for mycoplasma contamination. Cells were cultured in a 37 °C incubator with 5% CO_2. All cells were supplemented in Dulbecco's modified Eagle's medium (DMEM) with 10% fetal bovine serum (FBS), 100 U·mL^{-1} penicillin, and 100 μg·mL^{-1} streptomycin (all were from M&C Gene Technology Ltd., Beijing).

Dark Cytotoxicity and Phototoxicity. The dark and light cytotoxicity of **Ru2** and **Ru3** was studied by Cell Counting Kit-8 (CCK-8, Selleck Chemicals LLC). A549 cells were seeded in 96-well plates (NEST) at a density of 5000 cells per well in 100 μL overnight. Then, the cells were incubated for 24 h under strictly subdued light conditions with different concentrations of **Ru2** or **Ru3** ranging from 10 nM to 100 μM. The cells were subsequently irradiated with a 300 W Xe lamp using a 500 nm bandpass filter to give a power density of 0.80 mW·cm^{-2} for 0, 1, or 10 min (corresponding to 0, 0.048, or 0.48 J·cm^{-2}, respectively) and were incubated for 24 h in the dark. Cell viabilities were detected by Cell Counting Kit-8 (CCK-8). IC_{50} values were calculated using Origin software.

Confocal Microscopy. A total of 200 000 A549 cells were seeded in a 35 mm laser confocal Petri dish (NEST) in 2 mL of DMEM with 10% FBS and incubated in a 37 °C incubator with 5% CO_2 for 24 h. Then, the cells were refreshed in phosphate-buffered saline (PBS) and incubated with 5 μM **Ru2** or **Ru3** at 37 °C for 4 h. Afterward, the cells were washed twice with PBS and incubated with Hoechst 33342 (DOJINDO), Lyso-Tracker Red (Beyotime), ER-Tracker Red (Beyotime), or MitoRed (KeyGEN BioTECH) for 30 min. The cells were then imaged on a Zeiss LSM880 fluorescence confocal microscope.

Detection of Lysosomal Damage. A549 cells were seeded in 24-well plates (NEST) at a density of 50 000 cells per well in 1 mL overnight. Then, the cells were stained with **Ru2** or **Ru3** (5, 10, 20, or 40 μM, respectively) for 4 h and irradiated with a 500 nm light of 0.80 mW·cm^{-2} for 6 min (0.288 J·cm^{-2}). After 24 h incubation, cells were washed with PBS and stained with Lyso-Tracker Red (Beyotime). Cells were then monitored by flow cytometry.

Annexin V-PE/7-AAD Apoptosis Assay. A549 cells were seeded in 24-well plates (NEST) at a density of 50 000 cells per well in 1 mL overnight. Then, the cells were stained with **Ru2** or **Ru3** (5, 10, or 20 μM, respectively) for 4 h and irradiated with a 500 nm light of 0.80 mW·cm^{-2} for 3 min (0.144 J·cm^{-2}). After 24 h incubation, cells were washed with PBS and stained with Annexin V-PE and 7-AAD (Bioss). Cells were then monitored by flow cytometry.

Mitochondria Membrane Potential (MMP) Detection. A549 cells were seeded in 24-well plates (NEST) at a density of 50 000 cells per well in 1 mL overnight. Then, the cells were stained with **Ru2** or **Ru3** (5, 10, or 20 μM, respectively) for 4 h and irradiated with a 500 nm light of 0.144 J·cm^{-2}. After 6 h incubation, cells were washed with PBS and stained with tetramethylrhodamine ethyl ester (TMRE, BestBio) for 15 min. Cells were then detected by flow cytometry. Data were processed using Origin software.

https://dx.doi.org/10.1021/acsabm.0c00647
ACS Appl. Bio Mater. 2020, 3, 6025−6038

RESULTS AND DISCUSSION

Electronic Absorption. The UV−vis absorption spectra of **Ru1**−**Ru3** in acetonitrile are displayed in Figure 1, and the

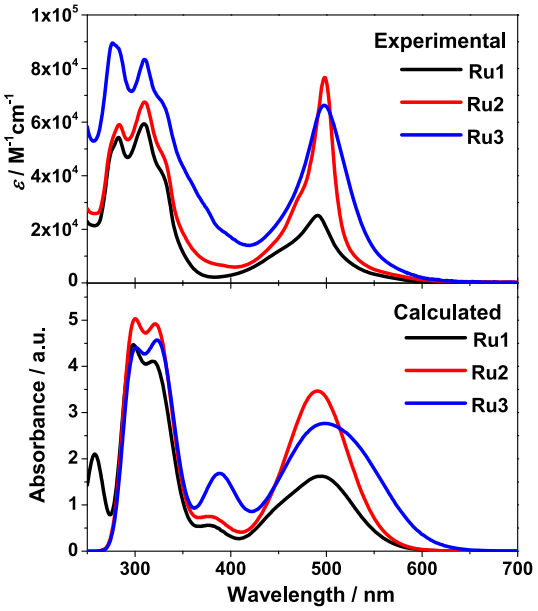

Figure 1. Experimental (upper panel) and calculated (lower panel) UV−vis absorption spectra of **Ru1**−**Ru3** in acetonitrile at room temperature. Calculations were performed using the TDDFT method with PBE1 functional and LANL2DZ/6-31G* basis set. The calculated spectra were red-shifted by 0.40 eV for better match with the experimental spectra.

normalized spectra in different solvents are shown in Figure S3 of the Supporting Information. The absorption band maxima and molar extinction coefficients in acetonitrile are summarized in Table 1. All complexes displayed well-resolved

Table 1. Photophysical Parameters for Complexes Ru1−Ru3 in Acetonitrile

	λ_{abs}/nm ($\log \varepsilon$/L·mol^{-1}·cm^{-1})[a]	λ_{em}/nm; Φ_{em}[b]	$\lambda_{T_1-T_n}$/nm (τ_T/μs)[d]	Φ_Δ[f]
Ru1	282 (4.74), 309 (4.78), 491 (4.41)	551 (648[c]); 0.0024	603 (−)[e]	0.05
Ru2	283 (4.77), 310 (4.84), 498 (4.98)	513; 0.0051	425 (27.2), 622 (31.0)	0.23
Ru3	277 (4.95), 310 (4.92), 498 (4.82)	525, 668; 0.0011	420 (0.91), 520 (0.63, 79.2), 578 (1.12)	0.13

[a]Absorption band maxima (λ_{abs}) and molar extinction coefficients ($\log \varepsilon$) at room temperature. [b]Emission band maxima (λ_{em}) and quantum yields (Φ_{em}) at room temperature, λ_{ex} = 436 nm, $c = 1 \times 10^{-5}$ mol L^{-1}. The reference used was a degassed acetonitrile solution of $[Ru(bpy)_3]Cl_2$ (Φ_{em} = 0.097, λ_{ex} = 436 nm). The emission lifetimes were too short or the signals were too weak to allow for the lifetimes to be measured on our LP920 instrument. [c]Emission wavelength upon excitation at 491 nm. [d]Nanosecond TA band maxima ($\lambda_{T_1-T_n}$) and triplet excited state lifetimes (τ_T) were measured at room temperature. [e]The τ_T of **Ru1** was too short to be reliably determined on our instrument. [f]The singlet oxygen quantum yield upon excitation at 355 nm (A_{355} = 0.5 in a 1 cm cuvette). $[Ru(bpy)_3]Cl_2$ in aerated CH_3CN (Φ_Δ = 0.57) was used as the reference.

absorption bands in the regions of 250−400 nm, which are assigned to ligand-localized spin-allowed $^1\pi,\pi^*$ transitions. In contrast, the poorly resolved absorption bands in the regions of 400−600 nm are tentatively attributed to charge-transfer transitions (metal-to-ligand charge transfer (^{1}MLCT), ligand-to-metal charge transfer (^{1}LMCT), ligand-to-ligand charge transfer (^{1}LLCT), or intraligand charge transfer (^{1}ILCT)) mixed with $^1\pi,\pi^*$ transitions. For **Ru1**−**Ru3**, the energies of these low-energy absorption bands are quite similar. However, the molar extinction coefficients are drastically larger in **Ru2** and **Ru3** compared to that in **Ru1**. Moreover, this band in **Ru2** is sharper, while in **Ru3** is broader. This difference should originate from the BODIPY-localized $^1\pi,\pi^*$ transition at ca. 480 nm in both **Ru2** and **Ru3**. In **Ru3**, the broadened absorption band at the longer wavelength side should be attributed to the ^{1}ILCT transition from the pyren-1-yl-based π orbital to the π^* orbital localized on the tpy on which pyren-1-yl is attached. This attribution is supported by the similar energy of the ^{1}ILCT transition in the Ir(III) complexes bearing pyren-1-yl-substituted tpy ligands.[35] Additional evidence supporting the aforementioned assignments comes from the TDDFT calculation results (Supporting Information Figure S4), from which the resultant natural transition orbitals (NTOs) (Tables 2 and S1−S3) confirmed the assignments discussed above. For example, the electron density of the holes for the S_5 state in **Ru1**, S_6 state in **Ru2**, and S_2 state in **Ru3** are distributed on the Ru(II) ion and the 4′-phenylpyridine or 4′-(pyren-1-yl)pyridine component on the R_1-tpy or R_2-tpy ligand, while the electron density distributions of the electrons are delocalized on the Ru(II) ion and the same tpy ligand where R_1 or R_2 is attached. These distributions resulted in transitions with mixed ^{1}ILCT/^{1}MLCT/^{1}LMCT/$^1\pi,\pi^*$ configurations. For the S_{10} state in **Ru1**, S_{14} state in **Ru2**, and S_{17} state in **Ru3**, the holes are mainly on the Ru(II) ion and the tpy ligand that has the R_1 substituent attached, whereas the electrons are delocalized on the metal and both tpy ligands, leading to ^{1}LLCT/^{1}MLCT/^{1}LMCT/$^1\pi,\pi^*$ transitions. For **Ru2** and **Ru3** that bear the BODIPY component, $^1\pi,\pi^*$ transitions localized on the BODIPY motif, i.e., S_7 state in **Ru2** and S_8 state in **Ru3**, are also major contributors to the low-energy absorption bands in these two complexes.

Photoluminescence. The steady-state emission spectra of complexes **Ru1**−**Ru3** were measured in acetonitrile, THF (with 5% acetonitrile), dichloromethane (with 5% acetonitrile), and toluene (with 10% acetonitrile) at room temperature, and the normalized spectra are illustrated in Figures 2 and S5. The emission maxima (λ_{em}) and quantum yields (Φ_{em}) are summarized in Tables 1 and S4. All three complexes exhibited very weak emission in all solvents used, with a quantum yield being varied between 0.11% and 7.50%. Upon 436 nm excitation, the emission of all complexes in acetonitrile was dominated by the green emission and the emission quantum yields were the lowest. However, the emission in the other solvents (i.e., THF, dichloromethane, and toluene) became stronger and exhibited dual emission, especially in toluene, in which the red emission at 652 nm for **Ru1** was the dominant one. In contrast, when excited at 491 nm, **Ru1** in acetonitrile gave rise to a very weak emission at 648 nm, and its lifetime was too short (<10 ns) to be measured on our instrument. Comparing the 648 nm emission of **Ru1** to that from the parent complex $[Ru(Ph\text{-}tpy)_2]^{2+}$ (τ = 1 ns),[14] the similar emission energy, short lifetime, and featureless emission profile imply that this emission likely originated from the

https://dx.doi.org/10.1021/acsabm.0c00647
ACS Appl. Bio Mater. 2020, 3, 6025−6038

Table 2. NTOs of the Major Transitions Contributing to the Absorption Band of 400−600 nm, Calculated Using the TDDFT Method with PBE1 Functional and LANL2DZ/6-31G* Basis Set in Acetonitrile

	Excited States and Properties[a]	Hole	Electron
Ru1	S_5 430 nm (499 nm) *f=0.500*	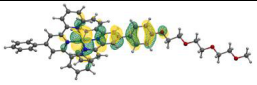 60% 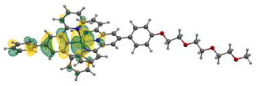 37%	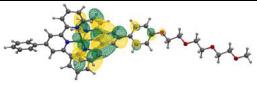 60% 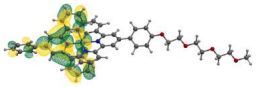 37%
	S_{10} 391 nm (447 nm) *f=0.202*	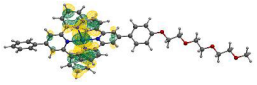	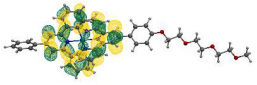
Ru2	S_6 430 nm (499 nm) *f=0.571*	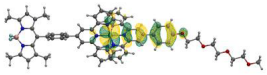 56% 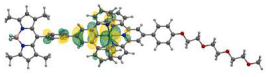 41%	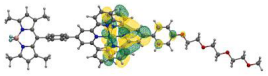 56% 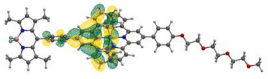 41%
	S_7 421 nm (487 nm) *f=0.583*	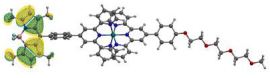	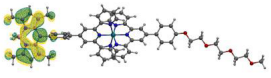
	S_{14} 391 nm (447 nm) *f=0.227*	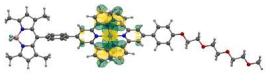	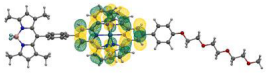
Ru3	S_2 457 nm (536 nm) *f=0.565*	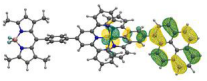	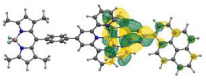
	S_8 421 nm (487 nm) *f=0.589*	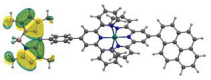	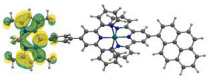
	S_9 417 nm (481 nm) *f=0.112*	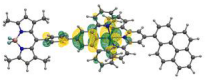	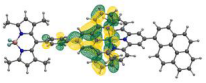
	S_{17} 391 nm (448 nm) *f=0.238*	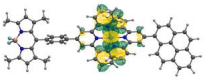	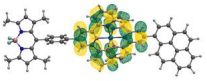

[a]Wavelengths in parentheses represent the wavelengths after a 0.4 eV red shift for better comparison with the experimental data.

similar emitting state to that for $[Ru(Ph\text{-}tpy)_2]^{2+}$, i.e., the fast-decayed ^{3}MLCT state. In addition, the NTOs shown in Table 3 indicate that the T_1 state of **Ru1** also has ^{3}ILCT/$^3\pi,\pi^*$/^{3}LMCT characters. For the green emission obtained at 436 nm excitation, we speculate it being the fluorescence from the ^{1}MLCT/^{1}LMCT/^{1}ILCT/$^1\pi,\pi^*$ state.

For **Ru2** and **Ru3**, the short-wavelength emission upon 436 nm excitation appeared to be a mirror image to the lowest-energy absorption band. Considering the involvement of $^1\pi,\pi^*$ transition of BODIPY in these absorption bands of these two complexes and the fluorescence of BODIPY, the emission bands at ca. 520 nm in **Ru2** and **Ru3** can be assigned to fluorescence from the $^1\pi,\pi^*$ state of BODIPY. **Ru2** and **Ru3** also possessed another weak emission band at 650−670 nm in almost all solvents tested except for **Ru2** in acetonitrile. Considering the similar energy of this emission band in **Ru2** and **Ru3** to the red-emission band in **Ru1** (648 nm), this band is tentatively assigned to the ^{3}MLCT/^{3}ILCT/$^3\pi,\pi^*$/^{3}LMCT states for **Ru2** and **Ru3**. Such attribution is supported by the NTOs of the T_2 states of **Ru2** and **Ru3** (see Table 3), which have a similar energy to the emitting T_1 state of **Ru1**. Although very rare, emission emanating from a higher triplet excited state has been reported for some Ru(II) tris-diimine complexes.[19,20,58] Dual emission was also previously reported for Ru(II) tris-diimine complexes.[25,26,59]

Transient Absorption (TA). Because the emitting state might not be the lowest triplet excited state (T_1) in some transition-metal complexes,[19,20,58,60,61] including some Ru(II)

https://dx.doi.org/10.1021/acsabm.0c00647
ACS Appl. Bio Mater. 2020, 3, 6025−6038

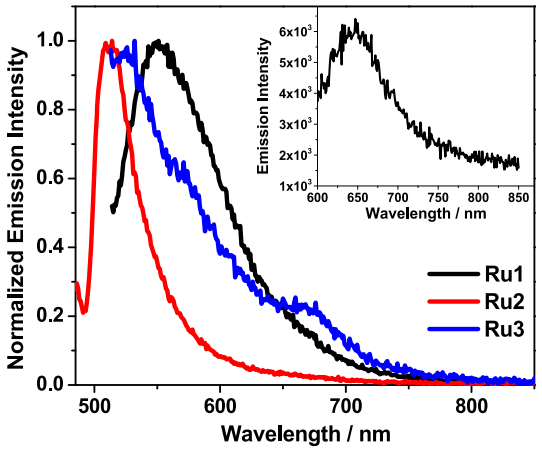

Figure 2. Normalized experimental emission spectra of **Ru1**−**Ru3** in deaerated acetonitrile at room temperature when excited at 436 nm. The inset shows the emission spectrum of **Ru1** in deaerated acetonitrile ($c = 5 \times 10^{-5}$ mol·L^{-1}) upon excitation at 491 nm.

complexes,[19,20,58,59] we conducted the nanosecond TA measurements to understand the T_1-state characteristics of **Ru1**−**Ru3**. The time-resolved TA spectra upon 355 nm excitation for these complexes are displayed in Figure 3, and the TA band maxima and T_1-state lifetimes deduced from the decay of TA signals are compiled in Table 1.

As shown in Figure 3, all complexes possessed similar TA spectral features with bleaching occurring in the regions of 440−530 nm (which are consistent with their ^{1}CT/$^1\pi,\pi^*$ absorption bands in their corresponding UV−vis absorption spectra) and broad positive absorption bands at 530−800 nm. In view of the similarly short (<10 ns) TA and emission lifetimes for **Ru1** and the similar spectral feature to the other reported Ru(tpy)(N^N^N)$^{2+}$ complexes,[20] we assign the observed TA spectrum of **Ru1** to its ^{3}MLCT/^{3}ILCT/$^3\pi,\pi^*$/^{3}LMCT state that emits. For **Ru2**, the TA signals were much stronger and longer-lived (ca. 30 μs) and the TA spectral feature resembled those of the BODIPY-pendant complexes reported in the literature.[26,31,32] Therefore, the origin of the TA is attributed to the BODIPY-centered $^3\pi,\pi^*$ excited state. The NTOs displayed in Table 3 indicate that the T_1 state of **Ru2** is exclusively localized on the BODIPY component. Thus, the observed TA of **Ru2** emanated from its long-lived T_1 state.

The TA of **Ru3** comprised two components with significant distinctions in spectral feature and lifetime. The spectral feature of the relatively short-lived TA component resembled more that of **Ru1**, but its lifetime was longer than that of **Ru1**. Considering the similar ^{3}MLCT/^{3}ILCT/$^3\pi,\pi^*$/^{3}LMCT nature of the T_2 state of **Ru3** to that of the T_1 sate of **Ru1**, we tentatively attribute this shorter-lived component to the T_2 state of **Ru3**. Its longer lifetime could be ascribed to the admixture of the pyrene-localized $^3\pi,\pi^*$ configuration in the emitting T_2 state of **Ru3**. Determination of this T_2-state lifetime by the decay of TA signals but not by the decay of emission signals is likely due to the very weak red-emission signals. In contrast, the much longer-lived TA species (79.2 μs) gave rise to distinctively different TA signals, likely emanating from the BODIPY-localized $^3\pi,\pi^*$ state, which is the T_1 state of **Ru3**, as demonstrated by the NTOs shown in Table 3. The presence of long-lived T_1 states in **Ru2** and **Ru3** would benefit their application as PSs for PDT, which would be manifested in the following sections.

Singlet Oxygen Generation. It is well known that reactive oxygen species (ROS) such as singlet oxygen ($^1O_2$), superoxide anion ($O_2^{-\bullet}$), or hydroxy free radical ($^\bullet$OH) are the active species that kill the tumor cells during PDT via reacting with lipids, proteins, and/or nucleic acids to induce extensive tissue dysfunction and injury. The efficiency of a PS to generate ROS plays a key role in determining the outcome of PDT. For most of the reported PSs, $^1O_2$ produced via energy transfer from the T_1 sate of a PS to the ground-state oxygen (type II mechanism) is typically the major player in PDT. To evaluate the feasibility of **Ru1**−**Ru3** as PSs, electron paramagnetic resonance (EPR) spectroscopy, which is a powerful tool to detect ROS generation in solutions and in biological systems,[62] was applied to detect $^1O_2$ formation by these complexes. Because the $^1O_2$ generation is a bimolecular process, a PS with long-lived T_1 state is a prerequisite for efficient $^1O_2$ generation. Based on this criterion, **Ru1** with a short-lived T_1 state will not be able to act as a PS. Thus, only **Ru2** and **Ru3** were investigated for their $^1O_2$ generation.

Figure 4 displays the 4-OH-TEMPO adduct signals from the solutions of **Ru2** or **Ru3** in water/acetonitrile (1:4, v/v) with 100 mM 4-OH-TEMP (singlet oxygen trapper) after

Table 3. NTOs for the Triplet Excited State(s) (T_n) of Ru1−Ru3, Calculated with the PBE1 Functional and LANL2dz/6-31G* Basis Set in Acetonitrile

		HOTO	LUTO
Ru1	T_1 729 nm	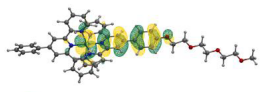	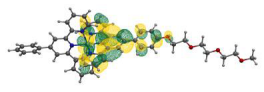
Ru2	T_1 852 nm	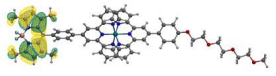	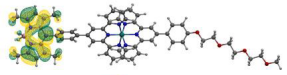
	T_2 739 nm	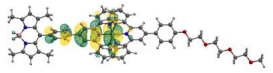	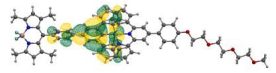
Ru3	T_1 850 nm	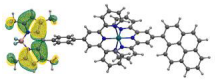	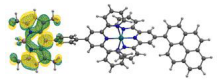
	T_2 713 nm	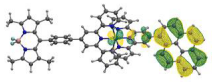	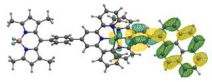

https://dx.doi.org/10.1021/acsabm.0c00647
ACS Appl. Bio Mater. 2020, 3, 6025−6038

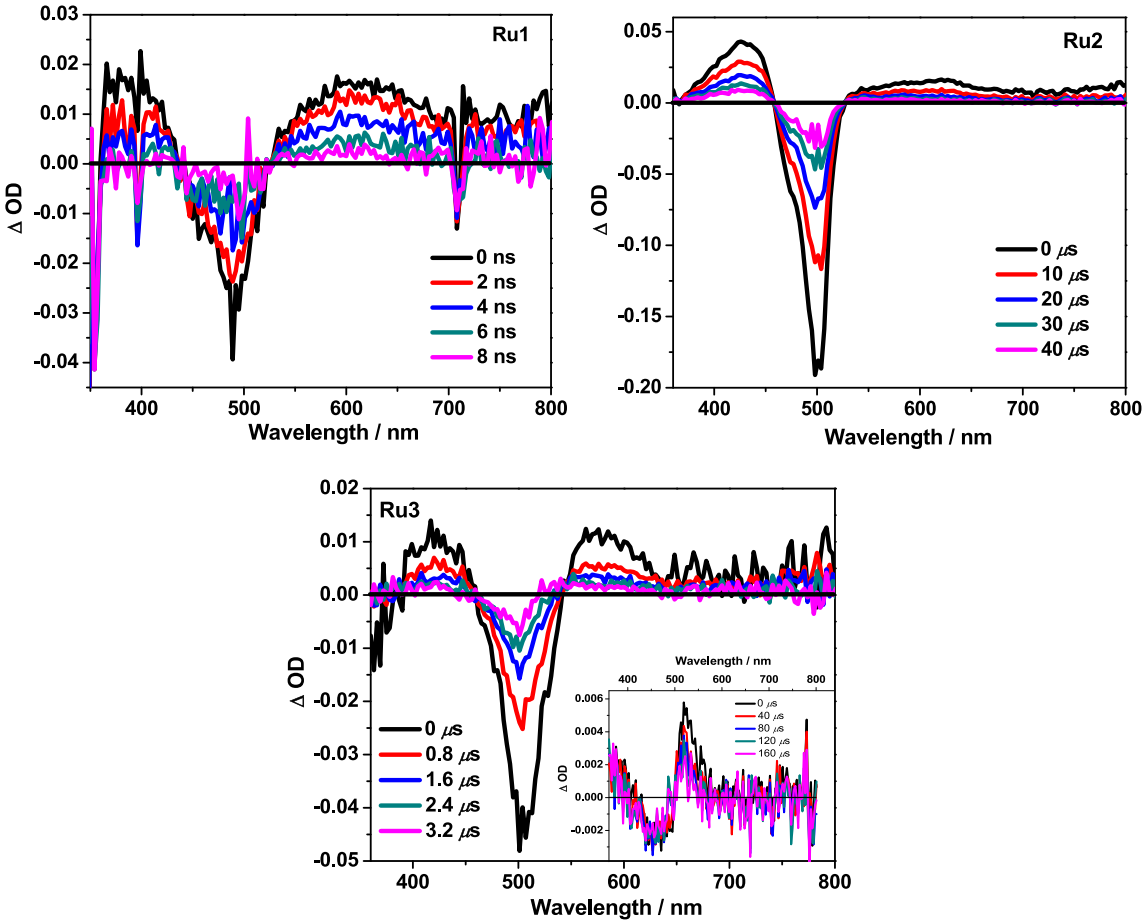

Figure 3. Time-resolved nanosecond transient difference absorption spectra of complexes **Ru1**−**Ru3** in deaerated acetonitrile at room temperature after 355 nm laser pulse excitation. A_{355} = 0.4 in a 1 cm cuvette.

irradiation with a 532 nm light of 200 mW·cm^{-2}. The 4-OH-TEMPO adduct signals in solutions with **Ru2** or **Ru3** were salient than those in the reference solution, indicating the generation of $^1O_2$ by these two complexes. The signal intensities increased with increased complex concentration and irradiation time. For solutions with the same concentration of complex (the PS) and the same irradiation time, the one with **Ru2** induced much stronger signals than the one with **Ru3**. The stronger signal induced by **Ru2** is attributed to its longer-lived triplet excited state, suggesting that **Ru2** could exhibit stronger phototoxicity and be a more efficient PS for PDT.

To quantitatively measure the $^1O_2$ generation efficiency of **Ru1**−**Ru3** in CH_3CN, the emission intensity of $^1O_2$ at 1270 nm was monitored and compared to that of the reference complex $[Ru(bpy)_3]Cl_2$ in CH_3CN (Φ_Δ = 0.57)[40] under identical excitation conditions. The obtained Φ_Δ values for these complexes are listed in Table 1, which follow the order **Ru2** > **Ru3** > **Ru1** and are consistent with the aforementioned trends observed for **Ru2** and **Ru3** from the EPR results.

(Photo)cytotoxicity. To demonstrate the feasibility of **Ru2** and **Ru3** as PSs for PDT, a human lung cancer cell line (A549) and the CCK-8 cell viability test kit were used to quantify their *in vitro* PDT effect. A549 cells were incubated for 24 h under strictly subdued light conditions with different concentrations of **Ru2** or **Ru3** ranging from 10 nM to 100 μM. Cells were subsequently irradiated with a 500 nm light of 0.80 mW·cm^{-2} for 0, 1, or 10 min (corresponding to 0, 0.048, or 0.48 J·cm^{-2} fluence) and were incubated for 24 h in dark conditions (Figure 5). The effective concentrations to reduce cell viability by 50% (EC_{50}) were then assessed for different conditions and are listed in Table 4. Both complexes exhibited weak dark cytotoxicity, but **Ru2** was slightly less toxic than **Ru3** without light irradiation. Upon 500 nm light irradiation, the toxicity of both complexes increased, manifesting the PDT effect. The EC_{50} value of **Ru2** with 0.48 J·cm^{-2} irradiation (i.e., 10 min irradiation) decreased to 1.50 μM, corresponding to a phototherapeutic index (PI) of 35.3, which is more phototoxic than **Ru3** (with an EC_{50} value of 7.41 μM and a PI value of 4.90) under the same PDT conditions. This result shows that **Ru2** can induce cell death more significantly than **Ru3** upon 500 nm light irradiation for 10 min, implying that **Ru2** is a better PS than **Ru3** upon 500 nm light activation toward A549 cells. This trend corresponds to the trend of $^1O_2$ generation efficiency (Table 1), suggesting that $^1O_2$ could be the major player in the PDT process of these complexes. Moreover, the PDT effects of both complexes are much stronger than the reported $[Ru(terpy)(terpy\text{-}X)]^{2+}$ (X = H, Cl, Br, OMe, COOH, COOMe, NMe_2) complexes upon 480 nm activation (3.1 J·cm^{-2}) toward Hela cells.[21]

Intracellular Distribution. Organelle targeting is an important property of photosensitizers relating to their induced cell death pathways and cytotoxicity efficacy. To identify the intracellular PDT mechanisms of these Ru(II) complexes, the localization of **Ru2** and **Ru3** in different cell organelles was investigated via confocal laser scanning

https://dx.doi.org/10.1021/acsabm.0c00647
ACS Appl. Bio Mater. 2020, 3, 6025−6038

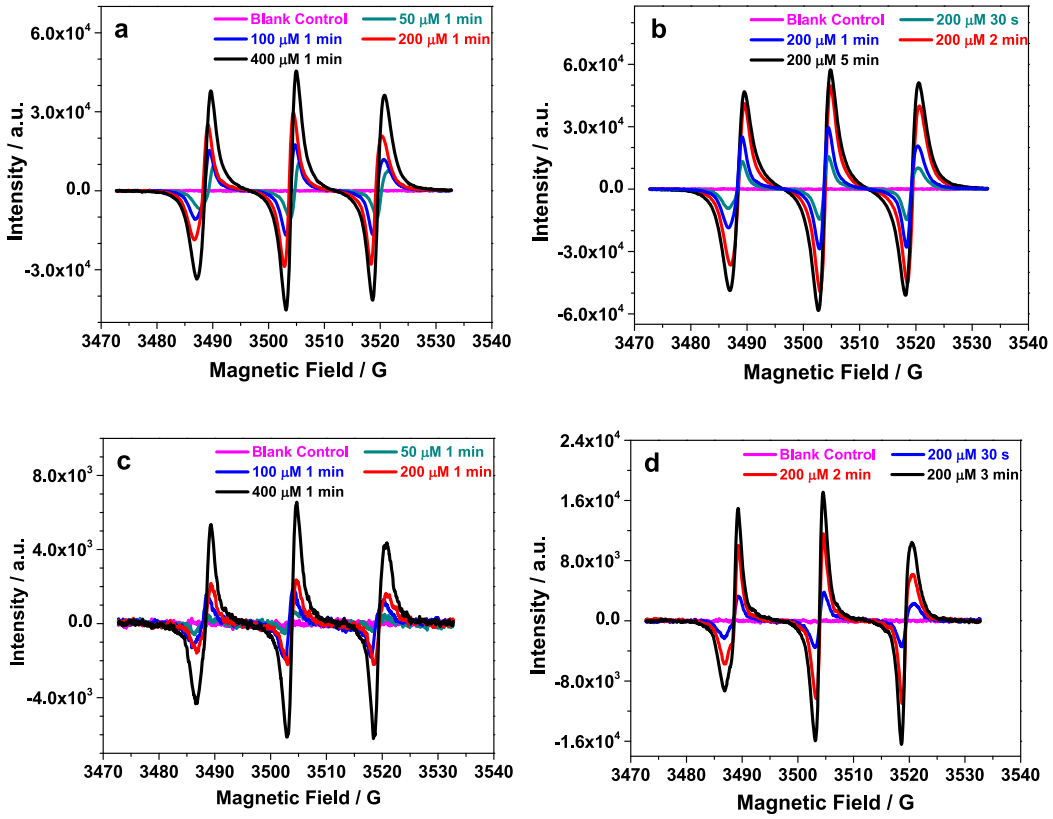

Figure 4. X band EPR spectra of complexes **Ru2** (a, b) and **Ru3** (c, d) with different concentrations or irradiation times. The complexes were dissolved in mixed water and acetonitrile (1:4, v/v) with 100 mM 4-OH-TEMP and irradiated with a 532 nm light of 200 mW·cm^{-2}.

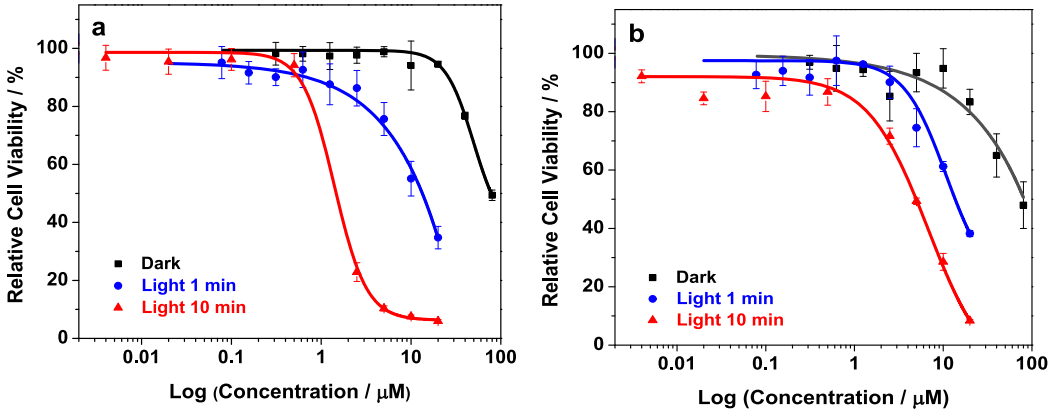

Figure 5. *In vitro* PDT dose–response curves for (a) **Ru2** and (b) **Ru3** toward A549 cells. The samples were treated with no light (black) or irradiated with 0.80 mW·cm^{-2} light for 1 min (blue) or 10 min (red).

Table 4. EC_{50} Values (μM) for Ru2 and Ru3 under Different Irradiation Conditions

	dark	light (1 min)[a]		light (10 min)[b]	
	EC_{50}	EC_{50}	PI[c]	EC_{50}	PI[c]
Ru2	53.0	23.9	2.22	1.50	35.3
Ru3	36.3	11.1	3.27	7.41	4.90

[a]Irridiated with a 500 nm light of 0.80 mW·cm^{-2} for 1 min. [b]Irridiated with a 500 nm light of 0.80 mW·cm^{-2} for 10 min. [c]Phototherapeutic index, PI = EC_{50} (dark)/EC_{50} (light).

microscopy (CLSM). A549 cells were stained with 5 μM **Ru2** or **Ru3** for 4 h and costained with different cell organelle trackers including Hoechst 33342[63] (blue tracker for the nucleus), Lyso-Tracker Red[64] (red tracker for the lysosome), ER-Tracker Red (red tracker for the endoplasmic reticulum), and MitoRed[65] (red tracker for mitochondria). Then, the cells were observed under confocal microscopy. As illustrated in Figure 6, the green emission from **Ru2** well overlapped with the red fluorescence from Lyso-Tracker Red but not with the emission of the nucleus tracker or ER-Tacker. These results imply that **Ru2** is mainly localized in the lysosomes. The aggregated spots that did not colocalize with lysosomes were probably either aggregates of **Ru2** attached to the plasma membrane or those inside the vesicles. Therefore, lysosomes could be crucial targets for PDT-induced cell death for **Ru2**. For **Ru3**, its intracellular emission was too weak to allow for a

https://dx.doi.org/10.1021/acsabm.0c00647
ACS Appl. Bio Mater. 2020, 3, 6025−6038

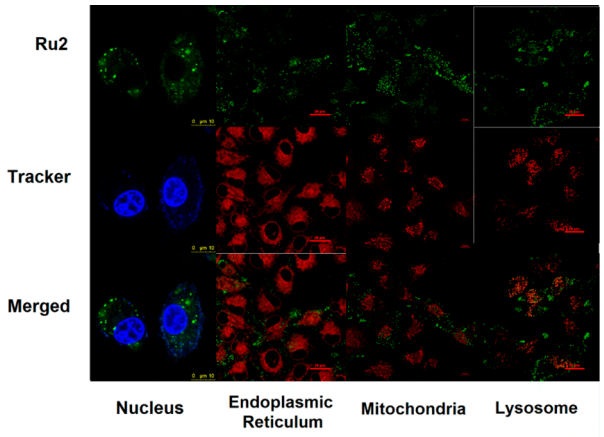

Figure 6. Fluorescence imaging of live A549 cells stained with **Ru2** (5 μM) and the related fluorescent dyes that target different organelles. **Ru2** was observed as bright green in the cytoplasm.

reliable determination of its intracellular localization with CLSM.

Lysosomal Damage. Lysosomes are not only an important organelle to recycle obsolete cellular molecules but also involved in various cellular processes including plasma membrane repair, apoptosis, cell signaling, and energy metabolism.[66] To confirm the important role of lysosomes in the pathway of PDT-induced cell death by **Ru2**, flow cytometry was applied to detect the photoinduced lysosomal damage by **Ru2**. A549 cells were stained with **Ru2** (5, 10, 20, and 40 μM, respectively) for 4 h and irradiated with a 500 nm light of 0.8 mW·cm^{-2} for 6 min (0.288 J·cm^{-2}), Lyso-Tracker Red was then applied to reflect the lysosomal damage. The fluorescence intensity of Lyso-Tracker Red correlates with the integrity of the lysosome membrane, i.e., the lower the Lyso-Tracker Red fluorescence intensity, the stronger the damage to the lysosome. As shown in Figure 7, 20 or 40 μM **Ru2** caused significant lysosomal damage. This result indicates that **Ru2** accumulated in lysosomes induced lysosomal damage upon light activation.

Mitochondrial Membrane Potential (MMP) Change. The CLSM results indicate that **Ru2** mainly accumulated in lysosomes after uptake by cells. However, mitochondria have been extensively involved in cell damage/death due to PDT treatment. To understand whether **Ru2**-mediated PDT caused

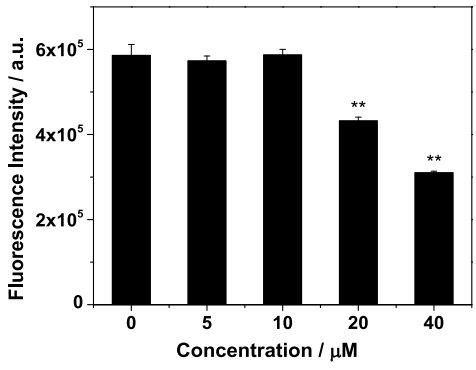

Figure 7. Quantitative column plot of the flow cytometry of lysosome damage detection. Data are plotted as the mean ± s.d.; n = 3 biologically independent samples. **P < 0.01 and versus dimethyl sulfoxide (DMSO) control.

mitochondria damage, changes in the mitochondrial membrane potential (MMP) were detected by flow cytometry via the TMRE test,[67] which is a cell permeant and positively charged dye readily accumulating in the negatively charged mitochondria. The MMP was characterized by the intensity of the orange-red fluorescence of TMRE along the x-axis, while mitochondria of decreased membrane potential failed to sequester TMRE. As shown in Figure 8, the decrease of

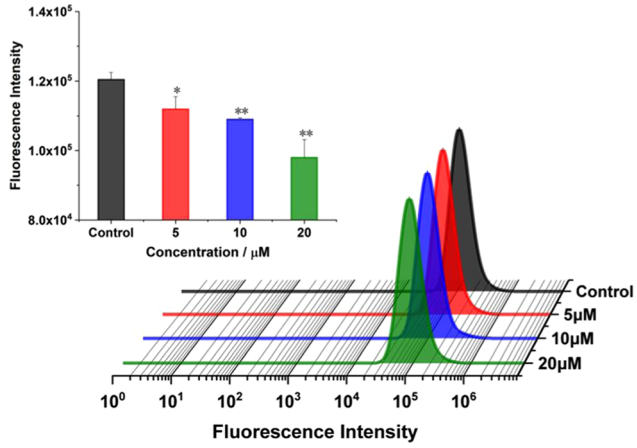

Figure 8. Contour plots for the flow cytometry results of A549 cells stained with TMRE 6 h after **Ru2**-PDT treatment. Fluorescence intensity of TMRE is shown on the x-axis, and **Ru2** concentration is displayed on the y-axis. The inset represents the quantitative column plots of the flow cytometry result. Data are plotted as the mean ± s.d.; n = 3 biologically independent samples. **P < 0.01 and versus DMSO control.

MMP was significant for the A549 cells, which were incubated with 5 or 20 μM **Ru2** and irradiated with a 500 nm light of 0.144 J·cm^{-2}. The higher the photosensitizer concentration, the greater the MMP decrease, which reflects the mitochondrial dysfunction during PDT.

The result indicates that mitochondrial damage occurred in the form of **Ru2**-induced cell death. However, the intracellular distribution experiment discussed earlier indicated that the lysosome was the direct target of the sensitizer and the distribution of **Ru2** in mitochondria was not obvious (Figure 6). Thus, there was no evidence to support direct mitochondrial damage by PDT of **Ru2**. In a previous report using phthalocyanine 4 (Pc4) as the sensitizer, lysosomal iron release induced PDT-mediated mitochondrial dysfunction and subsequent cell killing, probably through iron uptaking by the mitochondria and formation of ROS via the Fenton reaction.[68] Therefore, we speculate that mitochondrial damage is a secondary injury induced by lysosomal damage.

Cell Death Pathway. PDT can cause cell death through different pathways, e.g., autophagy, apoptosis, or necrosis, depending on factors including the nature and concentration of PSs, irradiation time, etc.[69] To explore the pathway of **Ru2**-induced cell death, flow cytometry was applied to identify the early apoptotic cells (Annexin V-PE+/7-AAD−) and the late apoptotic cells (Annexin V-PE+/7-AAD+) or necrotic cells (Annexin V-PE−/7-AAD+).[70] A549 cells were first stained with **Ru2** (5, 10, 20 μM) for 4 h and irradiated with a 500 nm light of 0.144 J·cm^{-2}. The PDT-treated cells were then incubated for 24 h under strictly subdued light conditions before detection. As shown in Figure 9, the percentages of late apoptotic cells represented in Q2 increased to 10, 13, and 19%

https://dx.doi.org/10.1021/acsabm.0c00647
ACS Appl. Bio Mater. 2020, 3, 6025−6038

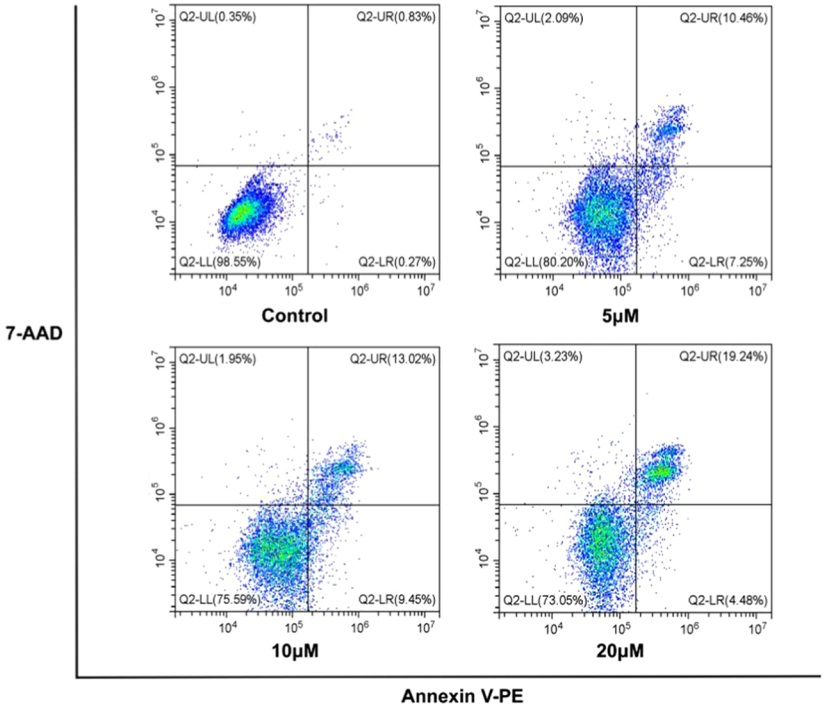

Figure 9. Flow cytometry of A549 cells cocultured with 5, 10, or 20 μM **Ru2**. The plot shows Annexin V-PE on the *x*-axis and 7-AAD on the *y*-axis.

upon treatment of 5, 10, and 20 μM **Ru2** and light, respectively. The higher the photosensitizer concentration, the more the cells underwent apoptotic death. This trend correlates well with the trends of $^1O_2$ generation and the cell viability studies discussed in the previous sections. Although the decreased MMP observed in Figure 8 is usually relevant to apoptosis, we believe that lysosomal damage upon light activation mainly drives the cells to apoptotic death considering the lack of distribution of **Ru2** in mitochondria. The exact mechanism of how lysosomal damage caused cell death and the role of mitochondrial dysfunction warrant further investigation.

CONCLUSIONS

Three Ru(II) bis-terpyridine complexes were synthesized, and their photophysics and *in vitro* PDT effects were investigated. By attaching π-conjugated BODIPY and/or pyrenyl motif to the terpyridine ligands, we were able to dramatically increase the absorptivity of the $Ru(R\text{-}tpy)_2^{2+}$ complexes in the green spectral regions (450−600 nm) and prolong the T_1-state lifetimes to tens of microseconds in **Ru2** and **Ru3**. The long-lived T_1 states in these two complexes promoted singlet oxygen generation upon green light excitation and consequently caused significant cell death toward the A549 lung cancer cell line. The PDT effect of **Ru2** was much stronger than that of **Ru3** due to its higher singlet oxygen generation ability. **Ru2** was found to mainly distribute in lysosomes. Upon 500 nm light activation, **Ru2** induced lysosomal damage and MMP decrease. The cell death pathway was predominantly via apoptosis. These preliminary results suggest that $Ru(R\text{-}tpy)_2^{2+}$-type complexes with appropriate π-conjugated pendants could act as long-wavelength activatable PSs.

ASSOCIATED CONTENT

Supporting Information

The Supporting Information is available free of charge at https://pubs.acs.org/doi/10.1021/acsabm.0c00647.

^{1}H NMR and high-resolution mass spectra of **Ru1**−**Ru3**, normalized UV−vis absorption and emission spectra of **Ru1**−**Ru3** in different solvents, comparison of the experimental and calculated absorption spectra of **Ru1**−**Ru3** in acetonitrile, NTOs of the major transitions contributing to the absorption bands at 280−600 nm for **Ru1**−**Ru3** in acetonitrile, and emission energies and quantum yields of **Ru1**−**Ru3** in different solvents (PDF)

AUTHOR INFORMATION

Corresponding Authors

Guoquan Liu − *State Key Laboratory of Natural and Biomimetic Drugs, School of Pharmaceutical Sciences, Peking University, Beijing 100191, P. R. China;* orcid.org/0000-0003-0680-4811; Email: guoquanliu@bjmu.edu.cn

Wenfang Sun − *Department of Chemistry and Biochemistry, North Dakota State University, Fargo, North Dakota 58108-6050, United States;* orcid.org/0000-0003-3608-611X; Phone: 701-231-6254; Email: Wenfang.Sun@ndsu.edu

Authors

Bingqing Liu − *Department of Chemistry and Biochemistry, North Dakota State University, Fargo, North Dakota 58108-6050, United States;* orcid.org/0000-0002-1540-2235

Yibo Gao − *State Key Laboratory of Natural and Biomimetic Drugs, School of Pharmaceutical Sciences, Peking University, Beijing 100191, P. R. China*

Mohammed A. Jabed − *Department of Chemistry and Biochemistry, North Dakota State University, Fargo, North Dakota 58108-6050, United States;* orcid.org/0000-0001-8552-0301

https://dx.doi.org/10.1021/acsabm.0c00647
ACS Appl. Bio Mater. 2020, 3, 6025−6038

Svetlana Kilina − *Department of Chemistry and Biochemistry, North Dakota State University, Fargo, North Dakota 58108-6050, United States;* orcid.org/0000-0003-1350-2790

Complete contact information is available at: https://pubs.acs.org/10.1021/acsabm.0c00647

Author Contributions

[§]B.L. and Y.G. contributed equally to this work.

Notes

The authors declare no competing financial interest.

■ ACKNOWLEDGMENTS

W.S. and S.K. are grateful to the National Science Foundation (NSF DMR-1411086 and CHE-1800476) for support regarding the syntheses, photophysical studies, or computational simulations for this work. S.K. also thanks to the Center for Computationally Assisted Science and Technology (CCAST) at North Dakota State University for providing computational resources and administrative support. G.L. acknowledges the support from the National Natural Science Foundation of China (31971173 and 91643112).

■ REFERENCES

(1) Monro, S.; Colón, K. L.; Yin, H.; Roque, J.; Konda, P.; Gujar, S.; Thummel, R. P.; Lilge, L.; Cameron, C. G.; McFarland, S. A. Transition Metal Complexes and Photodynamic Therapy from a Tumor-Centered Approach: Challenges, Opportunities, and Highlights from the Development of TLD1433. *Chem. Rev.* **2019**, *119*, 797−828.

(2) Celli, J. P.; Spring, B. Q.; Rizvi, I.; Evans, C. L.; Samkoe, K. S.; Verma, S.; Pogue, B. W.; Hasan, T. Imaging and Photodynamic Therapy: Mechanisms, Monitoring, and Optimization. *Chem. Rev.* **2010**, *110*, 2795−2838.

(3) Zamora, A.; Vigueras, G.; Rodríguez, V.; Santana, M. D.; Ruiz, J. Cyclometalated Iridium(III) Luminescent Complexes in Therapy and Phototherapy. *Coord. Chem. Rev.* **2018**, *360*, 34−76.

(4) Plaetzer, K.; Krammer, B.; Berlanda, J.; Berr, F.; Kiesslich, T. Photophysics and Photochemistry of Photodynamic Therapy: Fundamental Aspects. *Lasers Med. Sci.* **2009**, *24*, 259−268.

(5) Heinemann, F.; Karges, J.; Gasser, G. Critical Overview of the Use of Ru(II) Polypyridyl Complexes as Photosensitizers in One-Photon and Two-Photon Photodynamic Therapy. *Acc. Chem. Res.* **2017**, *50*, 2727−2736.

(6) Liu, J.; Zhang, C.; Rees, T. W.; Ke, L.; Ji, L.; Chao, H. Harnessing Ruthenium(II) as Photodynamic Agents: Encouraging Advances in Cancer Therapy. *Coord. Chem. Rev.* **2018**, *363*, 17−28.

(7) Poynton, F. E.; Bright, S. A.; Blasco, S.; Williams, D. C.; Kelly, J. M.; Gunnlaugsson, T. The Development of Ruthenium(II) Polypyridyl Complexes and Conjugates for in Vitro Cellular and in Vivo Applications. *Chem. Soc. Rev.* **2017**, *46*, 7706−7756.

(8) Shi, G.; Monro, S.; Hennigar, R.; Colpitts, J.; Fong, J.; Kasimova, K.; Yin, H.; DeCoste, R.; Spencer, C.; Chamberlain, L.; Mandel, A.; Lilgec, L.; McFarland, S. A. Ru(II) Dyads Derived from Alpha-Oligothiophenes: A New Class of Potent and Versatile Photosensitizers for PDT. *Coord. Chem. Rev.* **2015**, *282*−*283*, 127−138.

(9) Zeng, L.; Gupta, P.; Chen, Y.; Wang, E.; Ji, L.; Chao, H.; Chen, Z.-S. The Development of Anticancer Ruthenium(II) Complexes: From Single Molecule Compounds to Nanomaterials. *Chem. Soc. Rev.* **2017**, *46*, 5771−5804.

(10) Lazic, S.; Kaspler, P.; Shi, G.; Monro, S.; Sainuddin, T.; Forward, S.; Kasimova, K.; Hennigar, R.; Mandel, A.; McFarland, S.; Lilge, L. Novel Osmium-Based Coordination Complexes as Photosensitizers for Panchromatic Photodynamic Therapy. *Photochem. Photobiol.* **2017**, *93*, 1248−1258.

(11) Jain, A. Multifunctional, Heterometallic Ruthenium-Platinum Complexes with Medicinal Applications. *Coord. Chem. Rev.* **2019**, *401*, No. 213067.

(12) Zhang, P.; Sadler, P. J. Advances in the Design of Organometallic Anticancer Complexes. *J. Organomet. Chem.* **2017**, *839*, 5−14.

(13) Liang, J.-X.; Zhong, H.-J.; Yang, G.; Vellaisamy, K.; Ma, D.-L.; Leung, C.-H. Recent Development of Transition Metal Complexes with in vivo Antitumor Activity. *J. Inorg. Biochem.* **2017**, *177*, 276−286.

(14) Maestri, M.; Armaroli, N.; Balzani, V.; Constable, E. C.; Thompson, A. M. W. C. Complexes of the Ruthenium(II)-2,2′:6′,2″-terpyridine Family. Effect of Electron-Accepting and -Donating Substituents on the Photophysical and Electrochemical Properties. *Inorg. Chem.* **1995**, *34*, 2759−2767.

(15) Bhaumik, C.; Das, S.; Saha, D.; Dutta, S.; Baitalik, S. Synthesis, Characterization, Photophysical, and Anion-Binding Studies of Luminescent Heteroleptic Bis-Tridentate Ruthenium(II) Complexes Based on 2,6-Bis(Benzimidazole-2-yl)pyridine and 4′-Substituted 2,2′:6′,2″-Terpyridine Derivatives. *Inorg. Chem.* **2010**, *49*, 5049−5062.

(16) Breivogel, A.; Kreitner, C.; Heinze, K. Redox and Photochemistry of Bis(terpyridine)ruthenium(II) Amino Acids and Their Amide Conjugates − from Understanding to Applications. *Eur. J. Inorg. Chem.* **2014**, *2014*, 5468−5490.

(17) Balzani, V.; Juris, A. Photochemistry and Photophysics of Ru(II)-polypyridine Complexes in the Bologna Group. From Early Studies to Recent Developments. *Coord. Chem. Rev.* **2001**, *211*, 97−115.

(18) Jakubikova, E.; Chen, W.; Dattelbaum, D. M.; Rein, F. N.; Rocha, R. C.; Martin, R. L.; Batista, E. R. Electronic Structure and Spectroscopy of $[Ru(tpy)_2]^{2+}$, $[Ru(tpy)(bpy)(H_2O)]^{2+}$, and $[Ru(tpy)(bpy)(Cl)]^{+}$. *Inorg. Chem.* **2009**, *48*, 10720−10725.

(19) Wang, L.; Yin, H.; Jabed, M. A.; Hetu, M.; Monro, S.; Wang, C.; Kilina, S.; McFarland, S. A.; Sun, W.; et al. π-Expansive Heteroleptic Ruthenium(II) Complexes as Reverse Saturable Absorbers and Photosensitizers for Photodynamic Therapy. *Inorg. Chem.* **2017**, *56*, 3245−3259.

(20) Liu, Y.; Hammitt, R.; Lutterman, D. A.; Joyce, L. E.; Thummel, R. P.; Turro, C. Ru(II) Complexes of New Tridentate Ligands: Unexpected High Yield of Sensitized $^1O_2$. *Inorg. Chem.* **2009**, *48*, 375−385.

(21) Karges, J.; Blacque, O.; Jakubaszek, M.; Goud, B.; Goldner, P.; Gasser, G. Systematic Investigation of the Antiproliferative Activity of a Series of Ruthenium Terpyridine Complexes. *J. Inorg. Biochem.* **2019**, *198*, No. 110752.

(22) Zhao, R.; Hammitt, R.; Thummel, R. P.; Liu, Y.; Turro, C.; Snapka, R. M. Nuclear Targets of Photodynamic Tridentate Ruthenium Complexes. *Dalton Trans.* **2009**, 10926−10931.

(23) Constable, E. C. 2,2′:6′,2″-Terpyridines: From Chemical Obscurity to Common Supramolecular Motifs. *Chem. Soc. Rev.* **2007**, *36*, 246−253.

(24) McClenaghan, N. D.; Leydet, Y.; Maubert, B.; Indelli, M. T.; Campagna, S. Excited-State Equilibration: A Process Leading to Long-Lived Metal-to-Ligand Charge Transfer Luminescence in Supramolecular Systems. *Coord. Chem. Rev.* **2005**, *249*, 1336−1350.

(25) Lincoln, R.; Kohler, L.; Monro, S.; Yin, H.; Stephenson, M.; Zong, R.; Chouai, A.; Dorsey, C.; Hennigar, R.; Thummel, R. P.; McFarland, S. A. Exploitation of Long-Lived ^{3}IL Excited States for Metal−Organic Photodynamic Therapy: Verification in a Metastatic Melanoma Model. *J. Am. Chem. Soc.* **2013**, *135*, 17161−17175.

(26) Wang, J.; Lu, Y.; McGoldrick, N.; Zhang, C.; Yang, W.; Zhao, J.; Draper, S. M. Dual Phosphorescent Dinuclear Transition Metal Complexes, and Their Application as Triplet Photosensitizers for TTA Upconversion and Photodynamic Therapy. *J. Mater. Chem. C* **2016**, *4*, 6131−6139.

(27) Galletta, M.; Campagna, S.; Quesada, M.; Ulrich, G.; Ziessel, R. The Elusive Phosphorescence of Pyrromethene−BF_2 Dyes Revealed

in New Multicomponent Species Containing Ru(II)−Terpyridine Subunits. *Chem. Commun.* **2005**, *84*, 4222−4224.
(28) Galletta, M.; Puntoriero, F.; Campagna, S.; Chiorboli, C.; Quesada, M.; Goeb, S.; Ziessel, R. Absorption Spectra, Photophysical Properties, and Redox Behavior of Ruthenium(II) Polypyridine Complexes Containing Accessory Dipyrromethene-BF_2 Chromophores. *J. Phys. Chem. A* **2006**, *110*, 4348−4358.
(29) Passalacqua, R.; Loiseau, F.; Campagna, S.; Fang, Y.-Q.; Hanan, G. S. In Search of Ruthenium(II) Complexes Based on Tridentate Polypyridine Ligands That Feature Long-Lived Room-Temperature Luminescence: The Multichromophore Approach. *Angew. Chem., Int. Ed.* **2003**, *42*, 1608−1611.
(30) Majumdar, P.; Yuan, X.; Li, S.; Le Guennic, B.; Ma, J.; Zhang, C.; Jacquemin, D.; Zhao, J. Cyclometalated Ir(III) Complexes with Styryl-BODIPY Ligands Showing Near IR Absorption/Emission: Preparation, Study of Photophysical Properties and Application as Photodynamic/Luminescence Imaging Materials. *J. Mater. Chem. B* **2014**, *2*, 2838−2854.
(31) Liu, B.; Monro, S.; Jabed, M. A.; Cameron, C. G.; Colón, K. L.; Xu, W.; Kilina, S.; McFarland, S. A.; Sun, W. Neutral Iridium(III) Complexes Bearing BODIPY-Substituted N-Heterocyclic Carbene (NHC) Ligands: Synthesis, Photophysics, *In Vitro* Theranostic Photodynamic Therapy, and Antimicrobial Activity. *Photochem. Photobiol. Sci.* **2019**, *18*, 2381−2396.
(32) Rachford, A. A.; Ziessel, R.; Bura, T.; Retailleau, P.; Castellano, F. N. Boron Dipyrromethene (Bodipy) Phosphorescence Revealed in $[Ir(ppy)_2(bpy\text{-}C{\equiv}C\text{-}Bodipy)]^+$. *Inorg. Chem.* **2010**, *49*, 3730−3736.
(33) Majumdar, P.; Yuan, X.; Li, S.; Le Guennic, B.; Ma, J.; Zhang, C.; Jacquemin, D.; Zhao, J. Cyclometalated Ir(III) Complexes with Styryl-BODIPY Ligands Showing Near IR Absorption/Emission: Preparation, Study of Photophysical Properties and Application as Photodynamic/Luminescence Imaging Materials. *J. Mater. Chem. B* **2014**, *2*, 2838−2854.
(34) Jiang, X.; Peng, J.; Wang, J.; Guo, X.; Zhao, D.; Ma, Y. Iridium-based High-sensitivity Oxygen Sensors and Photosensitizers with Ultra-long Triplet Lifetimes. *ACS Appl. Mater. Interfaces* **2016**, *8*, 3591−3600.
(35) Liu, B.; Monro, S.; Li, Z.; Jabed, M. A.; Ramirez, D.; Cameron, C. G.; Colón, K.; Roque, J.; Kilina, S.; Tian, J.; McFarland, S. A.; Sun, W. New Class of Homoleptic and Heteroleptic Bis(terpyridine) Iridium(III) Complexes with Strong Photodynamic Therapy Effects. *ACS Appl. Bio Mater.* **2019**, *2*, 2964−2977.
(36) Peng, X.; Xu, Y.; Sun, S.; Wu, Y.; Fan, J. A Ratiometric Fluorescent Sensor for Phosphates: Zn^{2+}-Enhanced ICT and Ligand Competition. *Org. Biomol. Chem.* **2007**, *5*, 226−228.
(37) Jung, H. S.; Han, J.; Shi, H.; Koo, S.; Singh, H.; Kim, H. J.; Sessler, J. L.; Lee, J. Y.; Kim, J. H.; Kim, J. S. Overcoming the Limits of Hypoxia in Photodynamic Therapy: A Carbonic Anhydrase IX-Targeted Approach. *J. Am. Chem. Soc.* **2017**, *139*, 7595−7602.
(38) Demas, J. N.; Crosby, G. A. The Measurement of Photoluminescence Quantum Yields. A Review. *J. Phys. Chem. A* **1971**, *75*, 991−1024.
(39) Suzuki, K.; Kobayashi, A.; Kaneko, S.; Takehira, K.; Yoshihara, T.; Ishida, H.; Shiina, Y.; Oishi, S.; Tobita, S. Reevaluation of Absolute Luminescence Quantum Yields of Standard Solutions Using a Spectrometer with an Integrating Sphere and a Back-Thinned CCD Detector. *Phys. Chem. Chem. Phys.* **2009**, *11*, 9850−9860.
(40) Abdel-Shafi, A. A.; Beer, P. D.; Mortimer, R. J.; Wilkinson, F. Photosensitized Generation of Singlet Oxygen from Ruthenium(II)-Substituted Benzoaza-Crown-Bipyridine Complexes. *Phys. Chem. Chem. Phys.* **2000**, *2*, 3137−3144.
(41) Argaman, N.; Makov, G. Density Functional Theory: An Introduction. *Am. J. Phys.* **2000**, *68*, 69−79.
(42) Perdew, J. P.; Burke, K.; Ernzerhof, M. Generalized Gradient Approximation Made Simple. *Phys. Rev. Lett.* **1996**, *77*, 3865−3868.
(43) Hay, P. J.; Wadt, W. R. Ab Initio Effective Core Potentials for Molecular Calculations. Potentials for K to Au Including the Outermost Core Orbitals. *J. Chem. Phys.* **1985**, *82*, 299−310.
(44) Krishnan, R.; Binkley, J. S.; Seeger, R.; Pople, J. A. Self-Consistent Molecular Orbital Methods. XX. A Basis Set for Correlated Wave Functions. *J. Chem. Phys.* **1980**, *72*, 650−654.
(45) Barone, V.; Cossi, M.; Tomasi, J. Geometry Optimization of Molecular Structures in Solution by the Polarizable Continuum Model. *J. Comput. Chem.* **1998**, *19*, 404−417.
(46) Casida, M. E.; Jamorski, C.; Casida, K. C.; Salahub, D. R. Molecular Excitation Energies to High-Lying Bound States from Time-Dependent Density-Functional Response Theory: Characterization and Correction of the Time-Dependent Local Density Approximation Ionization Threshold. *J. Chem. Phys.* **1998**, *108*, 4439−4449.
(47) Kilina, S.; Kilin, D.; Tretiak, S. Light-Driven and Phonon-Assisted Dynamics in Organic and Semiconductor Nanostructures. *Chem. Rev.* **2015**, *15*, 5929−5978.
(48) Qi, S.-C.; Hayashi, J.-I.; Zhang, L. Recent Application of Calculations of Metal Complexes Based on Density Functional Theory. *RSC Adv.* **2016**, *6*, 77375−77395.
(49) Dutoi, A. D.; Head-Gordon, M. Self-Interaction Error of Local Density Functionals for Alkali−Halide Dissociation. *Chem. Phys. Lett.* **2006**, *422*, 230−233.
(50) Ruzsinszky, A.; Perdew, J. P.; Csonka, G. I.; Vydrov, O. A.; Scuseria, G. E. Density Functionals That Are One- and Two- Are Not Always Many-Electron Self-Interaction-Free, As Shown for H_2^+, He_2^+, LiH^+, and Ne_2^+. *J. Chem. Phys.* **2007**, *126*, No. 104102.
(51) Dreuw, A.; Head-Gordon, M. Single-Reference ab Initio Methods for the Calculation of Excited States of Large Molecules. *Chem. Rev.* **2005**, *105*, 4009−4037.
(52) Chai, J.-D.; Head-Gordon, M. Long-Range Corrected Hybrid Density Functionals with Damped Atom−Atom Dispersion Corrections. *Phys. Chem. Chem. Phys.* **2008**, *10*, 6615−6620.
(53) Fiorentini, V. V.; Baldereschi, A. Dielectric Scaling of the Self-Energy Scissor Operator in Semiconductors and Insulators. *Phys. Rev. B* **1995**, *51*, 17196−17198.
(54) Furche, F.; Ahlrichs, R. Adiabatic Time-Dependent Density Functional Methods for Excited State Properties. *J. Chem. Phys.* **2002**, *117*, 7433−7447.
(55) Martin, R. L. Natural Transition Orbitals. *J. Chem. Phys.* **2003**, *118*, 4775−4777.
(56) Frisch, M. J.; Trucks, G. W.; Schlegel, H. B.; Scuseria, G. E.; Robb, M. A.; Cheeseman, J. R.; Scalmani, G.; Barone, V.; Petersson, G. A.; Nakatsuji, H.; Li, X.; Caricato, M.; Marenich, A. V.; Bloino, J.; Janesko, B. G.; Gomperts, R.; Mennucci, B.; Hratchian, H. P.; Ortiz, J. V.; Izmaylov, A. F.; Sonnenberg, J. L.; Williams; Ding, F.; Lipparini, F.; Egidi, F.; Goings, J.; Peng, B.; Petrone, A.; Henderson, T.; Ranasinghe, D.; Zakrzewski, V. G.; Gao, J.; Rega, N.; Zheng, G.; Liang, W.; Hada, M.; Ehara, M.; Toyota, K.; Fukuda, R.; Hasegawa, J.; Ishida, M.; Nakajima, T.; Honda, Y.; Kitao, O.; Nakai, H.; Vreven, T.; Throssell, K.; Montgomery, J. A., Jr; Peralta, J. E.; Ogliaro, F.; Bearpark, M. J.; Heyd, J. J.; Brothers, E. N.; Kudin, K. N.; Staroverov, V. N.; Keith, T. A.; Kobayashi, R.; Normand, J.; Raghavachari, K.; Rendell, A. P.; Burant, J. C.; Iyengar, S. S.; Tomasi, J.; Cossi, M.; Millam, J. M.; Klene, M.; Adamo, C.; Cammi, R.; Ochterski, J. W.; Martin, R. L.; Morokuma, K.; Farkas, O.; Foresman, J. B.; Fox, D. J. *Gaussian 16*, revision B.01; Gaussian Inc.: Wallingford, CT, 2016.
(57) Humphrey, W.; Dalke, A.; Schulten, K. VMD: Visual Molecular Dynamics. *J. Mol. Graphics* **1996**, *14*, 33−38.
(58) Sun, Y.; Joyce, L. E.; Dickson, N. M.; Turro, C. Efficient DNA Photocleavage by $[Ru(bpy)_2(dppn)]^{2+}$ with Visible Light. *Chem. Commun.* **2010**, *46*, 2426−2428.
(59) McFarland, S. A.; Lee, F. S.; Cheng, K. A. W. Y.; Cozens, F. L.; Schepp, N. P. Picosecond Dynamics of Nonthermalized Excited States in Tris(2,2-bipyridine)ruthenium(II) Derivatives Elucidated by High Energy Excitation. *J. Am. Chem. Soc.* **2005**, *127*, 7065−7070.
(60) Liu, R.; Dandu, N.; Li, Y.; Kilina, S.; Sun, W. Synthesis, Photophysics and Reverse Saturable Absorption of Bipyridyl Platinum(II) Bis(arylfluorenylacetylide) Complexes. *Dalton Trans.* **2013**, *42*, 4398−4409.

https://dx.doi.org/10.1021/acsabm.0c00647
ACS Appl. Bio Mater. 2020, 3, 6025−6038

(61) Wang, C.; Lystrom, L.; Yin, H.; Hetu, M.; Kilina, S.; McFarland, S. A.; Sun, W. Increasing the Triplet Lifetime and Extending the Ground-State Absorption of Biscyclometalated Ir(III) Complexes for Reverse Saturable Absorption and Photodynamic Therapy Applications. *Dalton Trans.* **2016**, *45*, 16366−16378.
(62) Griendling, K. K.; Touyz, R. M.; Zweier, J. L.; Dikalov, S.; Chilian, W.; Chen, Y. R.; Harrison, D. G.; Bhatnagar, A. Measurement of Reactive Oxygen Species, Reactive Nitrogen Species, and Redox-Dependent Signaling in the Cardiovascular System: A Scientific Statement from the American Heart Association. *Circ. Res.* **2016**, *119*, 39−75.
(63) Chazotte, B. Labeling Nuclear DNA with Hoechst 33342. *Cold Spring Harbor Protoc.* **2011**, *2011*, 83−85.
(64) Lemieux, B.; Percival, M. D.; Falgueyret, J. P. Quantitation of the Lysosomotropic Character of Cationic Amphiphilic Drugs Using the Fluorescent Basic Amine Red DND-99. *Anal. Biochem.* **2004**, *327*, 247−251.
(65) Zhang, S.; Wu, W.; Wu, Y.; Zheng, J.; Suo, T.; Tang, H.; Tang, J. RNF152, a Novel Lysosome Localized E3 Ligase with Pro-Apoptoticactivities. *Protein Cell* **2010**, *1*, 656−663.
(66) Settembre, C.; Fraldi, A.; Medina, D. L.; Ballabio, A. Signals from the Lysosome: A Control Centre for Cellular Clearance and Energy Metabolism. *Nat. Rev. Mol. Cell Biol.* **2013**, *14*, 283−296.
(67) Jayaraman, S. Flow Cytometric Determination of Mitochondrial Membrane Potential Changes During Apoptosis of T Lymphocytic and Pancreatic Beta Cell Lines: Comparison of Tetramethylrhodamineethylester (TMRE), Chloromethyl-X-rosamine (H2-CMX-Ros) and MitoTracker Red 580 (MTR580). *J. Immunol. Methods* **2005**, *306*, 68−79.
(68) Hung, H.-I.; Schwartz, J. M.; Maldonado, E. N.; Lemasters, J. J.; Nieminen, A.-L. Mitoferrin-2-dependent Mitochondrial Iron Uptake Sensitizes Human Head and Neck Squamous Carcinoma Cells to Photodynamic Therapy. *J. Biol. Chem.* **2013**, *288*, 677−686.
(69) Donohoe, C.; Senge, M. O.; Arnaut, L. G.; Gomes-da-Silva, L. C. Cell Death in Photodynamic Therapy: From Oxidative Stress to Anti-Tumor Immunity. *Biochim. Biophys. Acta, Rev. Cancer* **2019**, *1872*, No. 188308.
(70) Yang, L.; Zhou, X.; Yang, J.; et al. Aspirin Inhibits Cytotoxicity of Prion Peptide PrP106-126 to Neuronal Cells Associated with Microglia Activation *In Vitro*. *J. Neuroimmunol.* **2008**, *199*, 10−17.

https://dx.doi.org/10.1021/acsabm.0c00647
ACS Appl. Bio Mater. 2020, 3, 6025−6038